Hindawi
Shock and Vibration
Volume 2019, Article ID 6515462, 21 pages
https://doi.org/10.1155/2019/6515462

Research Article

Behaviors of Thin-Walled Cylindrical Shell Storage Tank under Blast Impacts

Shengzhuo Lu,[1] **Wei Wang**,[2] **Weidong Chen**,[1] **Jingxin Ma**,[1] **Yaqin Shi**,[1] **and Chunlong Xu**[1]

[1]*College of Aerospace and Civil Engineering, Harbin Engineering University, Harbin 150001, China*
[2]*School of Civil Engineering, Harbin Institute of Technology, Harbin 150090, China*

Correspondence should be addressed to Shengzhuo Lu; lusz@hrbeu.edu.cn

Received 18 March 2019; Revised 20 June 2019; Accepted 7 July 2019; Published 14 August 2019

Academic Editor: Mohammad A. Hariri-Ardebili

Large steel storage tanks designed with long-span structures, employed for storing oil and fuel, have been widely used in many countries over the past twenty years. Most of these tanks are thin-walled cylindrical shells. Owing to the high risk of gas explosions and the resulting deaths, injuries, and economic losses, more thorough damage analyses of these large structures should be conducted. This study examines the structural response of a simplified steel storage tank under a blast impact, as calculated by the LS-DYNA software package. The numerical results are then compared with a scale-model experiment. On that basis, the simplified storage tank prototype, which has a $15 \times 10^4\ m^3$ capacity, is analyzed using numerical simulation. In this study, we address issues around the variation in structural responses—particularly of the failure mode, resultant displacement, structural energy, and dynamic strain under the impact. In addition, we also discuss the effects of varying the internal liquid level, constraint conditions, and blast intensity.

1. Introduction

In the past twenty years, explosions caused by combustible gas from oil, petroleum, or chemical products have been reported frequently, both in China and elsewhere. These disasters, which have caused severe casualties and considerable property damage, have typically occurred in tank farms and oil depots where many storage tanks can be damaged [1, 2].

In 2005, a combustible air cloud, with thickness reaching up to 2 meters, was formed in Buncefield Oil Storage Depot in Hempstead, Hertfordshire, United Kingdom. This combustible air cloud led to a terrible explosion, and 23 large atmospheric storage tanks were damaged in the accident. In order to avoid even more serious consequences, more than 2000 residents were forced to evacuate [3]. The Buncefield Oil Storage Depot explosion was the most serious hazardous accident in European industry. In 2009, another severe explosion accident occurred at the Caribbean Petroleum Refining and Oil depot in Puerto Rico where the serial explosions damaged 18 oil storage tanks [4]. According to the statistics of oil storage tanks accidents by Chang and Lin, explosions occurred 61 times in total out of 242 accidents from 1960 to 2003 [5]. The most common causes of accidents are fires and explosions, which accounts for 85% of the total accidents [6].

With large-scale competition between petroleum reserves in developed and developing countries, the space and capacity of the oil storage tanks are extended from a large to a superlarge scale. For example, tanks with capacities greater than $20 \times 10^4\ m^3$ and diameters greater than 100 m have been built in some countries in the Middle East and South America. In tank farms, steel storage tanks are designed as long-span and thin-walled structures [7–9]. The increasing scale of storage structures has prompted more serious damage and aggravates the consequences of an explosion [10, 11].

Recently, several studies have focused on the response and failure analysis of energy structures and facilities subjected to a blast load. Atkinson described the patterns of damage observed in buildings in the industrial estates around Buncefield [12], presenting methods for assessing the degree of external and internal damage. He also dealt with

failure modes and the ignition of various types of liquid storage tanks during vapor cloud explosions. Clubley investigated the effect of long-duration blast loads on the structural response of aluminum cylindrical shell structures containing varying fluid levels [13, 14]. In his research, a detailed nonlinear numerical model comprising of remapped Lagrangian methods was built to analyze localized plate buckling and deformation. The relative computational accuracy of the numerical model was compared with experimental results obtained at one of the world's most powerful air blast testing facilities. Mittal et al. studied the stress (including maximum hoop and shear stresses), water sloshing heights, and energy response of steel water storage tanks using three-dimensional finite element (FE) simulations developed with ABAQUS software [15]. This study considered several influence factors, specifically the tank aspect ratios, percentages of water stored in the tank, tank wall thicknesses, and boundary conditions. Zhang et al. investigated the gas blast pressure distribution on the surface of a 1000 m^3 spherical storage tank using the trinitrotoluene (TNT) equivalent method [16]. Chen et al. performed full-scale validation tests and numerical simulations of far-field air blast loading acting on deformable steel drums [17], aiming to investigate possible forensic methods for aiding incident investigations. Hu and Zhao built a computational fluid dynamics (CFD) model using FLUENT CFD software [18]. They simulated the explosion of a methane-air mixture in a small-scale cylindrical vessel and compared this simulation to an experiment to validate their CFD model for simulating gaseous explosions. With this validation, they carried out a series of CFD simulations to obtain the magnitude and distribution of the internal explosion loading on tanks while accounting for the influences of tank capacity, height/depth, roof forms, and other factors. Lv et al. developed a correlation for the explosion maximum overpressure in liquid natural gas (LNG) tank areas based on the momentum conservation equation [19] and deduced the correlation factors in explosion tests. Their correlation enables safety managers and fire rescue commanders to conveniently predict the LNG explosion maximum overpressure. Li et al. assessed effects on vented explosion pressure in and around the area of a tank group. For their research, they designed a series of tank layouts with different separation gaps [20, 21] and calculated the internal and external pressures subjected to different separation gaps. They also proposed equations for calculating the tank's pressure–time history duration and shape. Zhang et al. studied the propagation of blast shock waves via numerical methods [22], analyzing the stress and structure deformation of LNG tanks under an explosive TNT blast.

In earlier research, more attention was paid to storage tanks with slim cylindrical structures or on closed tanks with thick walls (like LNG storage tanks). Few studies have analyzed the dynamic responses of thin-walled structures having a diameter nearly the same as, or even larger than, their height (for example, large floating-roof storage tanks). Furthermore, there has been little analysis of the relationship between structural energy and dynamic response under blast impacts.

In this paper, we briefly introduce an explosion test for a simplified scaled model of a storage tank under blast loading conditions. Then, the experiment is simulated using nonlinear FE software LS-DYNA. The LS-DYNA simulation is validated by comparing the test and numerical results. Subsequently, the numerical model is then applied to a storage tank with a capacity of 15×10^4 m^3 and is used to analyze several damage features, such as failure mode, resultant displacement, structural energy, and dynamic strain in different simulation conditions.

2. Materials and Methods

2.1. Specimen Design and Test Setup. Based on a 5×10^4 m^3 storage tank structure in the Yi Zheng Oil Reserve Base in China, we designed a simplified specimen structure for blast loading tests. Figure 1 shows the size parameters of the specimen, and Tables 1 and 2 present its geometry and material properties, respectively. In addition, the specimen is filled with water to simulate oil or other liquid fuel.

The experiments discussed in this paper were conducted and analyzed at the Defense Antiknock Laboratory at the Harbin Institute of Technology. Figure 2 shows a schematic of the principal test facility. The facility consists of the blast loading system and the platform. The blast comes from the ignition of air and acetylene combustible gas. Before the test, the gas fills a premixed container from each gas tank and is ignited by pressing the "start" button on the control panel. The burning combustible gas spreads through two connected parts: a steel circular tube with a diameter of 0.057 m and length of 16.8 m that stimulates the blast wave in a blast loading system and a steel cylindrical nozzle that is used to widen the impact area on the specimen. Quickly, the blast wave sprays and impacts the test specimen, as shown in Figure 2.

In the experiment, high-frequency piezoresistive pressure sensors were used to capture the blast loading and also to trigger the data acquisition system by the instrument 1# with sampling rate setting of 1 MHz as shown in Figure 2. Three pressure gauges, A, B, and D, were installed on the surface toward the blast side to measure the blast impact on the outer surface of the structure. Figures 3(a) and 3(b) display the distribution of pressure gauges on the test specimen. Besides, six strain gauges (S1-S6) were installed on the wall of the specimen to measure its dynamic response, as shown in Figures 3(a) and 3(c). These gauges were connected with data acquisition systems. Their signals were acquired by 2# instrument as well as acquiring system, and the sampled signal is 100 MHz.

2.2. Numerical Simulation and Validation. In this section, we describe the FE model of the test specimen built using LS-DYNA code. In addition, we verify the accuracy of the model with the scale-model test results. Thus, the FE model is used to validate the analytical model in the next sections.

The shell element SHELL163 in LS-DYNA was adopted for the wall and bottom plate of the specimen. SHELL163 is an explicit structural thin shell element with bending and

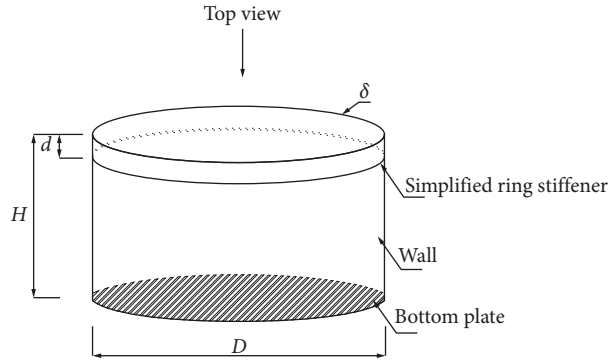

Figure 1: Configuration of the test specimen.

Table 1: Dimension of the test specimen.

Specimen	Dimension (D, mm)	Height (H, mm)	Thickness (δ, mm)	Water height (mm)	Distance (d, mm)
Simplified storage tank	923	297	1.2	260	35

Table 2: Material properties of the test specimen.

Specimen	Material	E (GPa)	f_y (MPa)	f_u (MPa)	Simplified ring stiffener (Φ8 reinforce)			
					Material	E (GPa)	f_y (MPa)	f_u (MPa)
Simplified storage tank	Q235-A	206	310	—	Q235	206	310	—

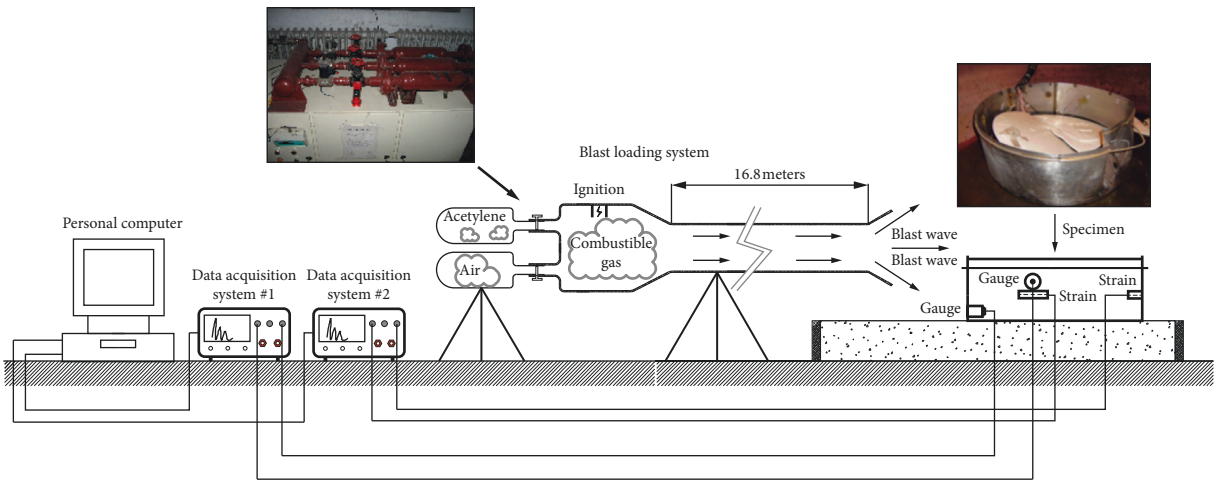

Figure 2: Schematic diagram of test setup.

membrane properties, and it supports nonlinear properties in the explicit dynamic analysis. This element can reduce computing time compared with a solid element. The eight-node solid element SOLID164 was adopted as a simplified ring stiffener, water, air, and high-explosive material. The Eulerian formulation, which is ideal for modeling fluid problems, was applied to the water, air, and high-explosive material in the FE model. The Lagrange formulation, which is generally suitable for elements without severe distortion, was applied to the other elements. The penalty fluid-structure coupling method in LS-DYNA was used to model the interactions between the simplified tank and blast wave from high explosive material, as well as between the water and the simplified tank.

The isotropic hardening plasticity material model in LS-DYNA was used to simulate the corresponding Q235 steel. This model is very cost effective and is available for shell and solid elements. In this material model, the strain rate effect was considered using the Cowper–Symonds model, which scales the yield stress using a strain rate dependent factor, as shown in the following equation:

$$\sigma_y\left(\varepsilon_{\text{eff}}^P, \dot{\varepsilon}_{\text{eff}}\right) = \sigma_y\left(\varepsilon_{\text{eff}}^P\right)\left[1 + \left(\frac{\dot{\varepsilon}_{\text{eff}}^P}{C}\right)^{1/P}\right], \quad (1)$$

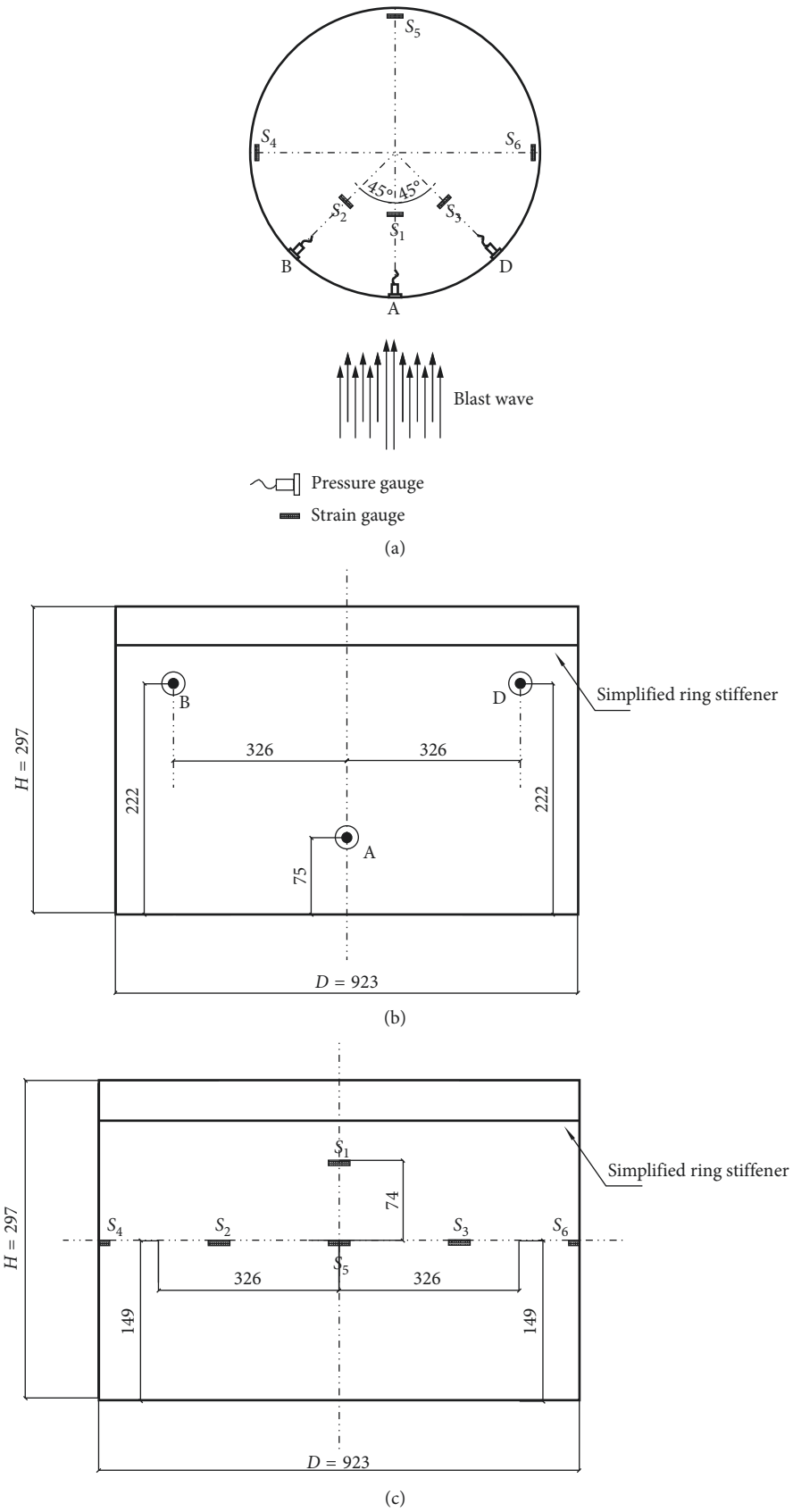

Figure 3: Distribution of pressure gauges and strain gauges. (a) Top view of the test specimen. (b) Distribution of pressure gauges. (c) Distribution of strain gauges.

where $\sigma_y(\varepsilon_{\text{eff}}^P)$ is the yield stress without strain rate effects, $\varepsilon_{\text{eff}}^P$ is the effective plastic strain rate, and C and P are the strain rate parameters, which were set to 40 and 5, respectively, for Q235 steel in this study.

The null material model is used to describe the deviatoric responses of air and water. The linear polynomial state equation used to simulate the volumetric response of air is given by

$$P = C_0 + C_1\mu + C_2\mu^2 + C_3\mu^3 + \left(C_4 + C_5\mu + C_6\mu^2\right)\overline{E}, \quad (2)$$

where $\mu = (\rho/\rho_0) - 1$, ρ is the current density, ρ_0 is the initial density, $\overline{E}$ is the initial energy per unit reference volume, and C_0–C_6 are parameters of the state equation. The material properties of air are given in Table 3. The Gruneisen equation of state with cubic shock velocity–particle velocity (V_S–P_S), which is used to simulate the volumetric response of water, is given in the following equation:

$$P = \frac{\rho_0 C^2\mu\left[1 + (1 - \gamma_0/2)\mu - a/2\mu^2\right]}{\left[1 - (S_1 - 1)\mu - S_2\left(\mu^2/(\mu+1)\right) - S_3\left(\mu^3/(\mu+1)^2\right)\right]^2} + (\gamma_0 + a\mu)\overline{E}. \quad (3)$$

Equation (3) is used for compressed material. Equation (4) is for expanded material:

$$P = \rho_0 C^2\mu + (\gamma_0 + a\mu)\overline{E}, \quad (4)$$

where C is the intercept of the V_S–P_S curve; S_1, S_2, and S_3 are the coefficients of the slope of the V_S–P_S curve; γ_0 is the Gruneisen gamma; and a is the first-order volume correction to γ_0. The material properties of water are listed in Table 4.

In the FE model, the combustible gas mixture (acetylene and air) is considered to be equivalent to TNT. A high-explosive material model (∗MAT_HIGH_ EXPLOSIVE_ BURN) incorporating the Jones–Wilkins–Lee (JWL) equation of state is used to describe the material property of the equivalent TNT charge. The JWL equation defines pressure as a function of relative volume and internal energy per initial volume, as shown in the following equation:

$$P = A\left(1 - \frac{\omega}{R_1 V}\right)e^{-R_1 V} + B\left(1 - \frac{\omega}{R_2 V}\right)e^{-R_2 V} + \frac{\omega E}{V}, \quad (5)$$

where P is the blast pressure; E is the internal energy per initial volume; V is the initial relative volume; and ω, A, B, R_1, and R_2 are material constants. The values of parameters A, B, R_1, and R_2 are 0.3, 3.71, 0.00323, 4.15, and 0.95, respectively [23].

Figure 4 compares the dynamic pressure history between the experiment and the numerical simulation. The trend of the blast loading change in the numerical simulation is consistent with that of the experiment. The value of the peak pressure is lower than that of the experimental results, with less than 10% relative error. The difference is probably caused by the secondary chemical reaction after the explosion (i.e., gas combustion), as the released energy from the reaction is neglected in the simulation process. Compared with the experimental history curves, the simulation curves are smoother because the explosion reaction is accompanied by the phenomena of bright light and air ionization in the experiment. These phenomena directly influence the pressure sensor signal and are not accounted for in the numerical simulation.

Considering the action time of positive pressure, the difference between the simulation and experiment in Gauge A, shown in Figure 4(a), is greater than for the other two gauges, with a 12.8% relative error. The test specimen was located on concrete in the experiment, so the ground was established as a perfectly rigid material in the FE model and produced a strong reflected wave. For this reason, Gauge A was distributed in the normal reflection region and near the ground. The overlap of the reflected and incident waves extends the action time of positive pressure. Thus, the established FE model of the simplified storage tank under blast loading was verified through comparison between the experimental and FE results.

2.3. Numerical Model of Storage Tank Prototype. The main objective of this study is to develop an FE model to simulate the response of long-span storage tank prototype under a blast impact. Figure 5 shows a diagram of a simplified storage tank with $15 \times 10^4\,\text{m}^3$ storage capacity; its simplified numerical model in the LS-DYNA environment is shown in Figure 6.

In Figure 5, the size of the structure is $100\,\text{m} \times 22.5\,\text{m}$ (diameter $D \times$ total height H). The simplified structure consists of the following components: tank walls, tank floor plate, wind girders, and ring stiffeners. Eight tank walls form the whole tank body. The height of the first wall ($h_{1\text{st}}$) is 3 m, and the heights of all other walls ($h_{2\text{nd}}$ to $h_{8\text{th}}$) are 2.7 m. Figure 7 shows the wall distribution in the numerical model. The storage tank is filled with different levels of liquid to simulate actual storage tank conditions in an explosion. The numerical models consider the effect of gravity. Figure 8 shows the liquid level conditions in the numerical simulation.

In the simulation model of the prototype tank, shell element SHELL163 is also used to simulate the tank wall and the bottom plate. More than 177,800 shell elements were built to simulate the storage tank structure in the model, and more than 1800,000 SOLID164 solid elements were built for simplified wind girders, water, air, and high-explosive material models. The Eulerian and Lagrangian formulations were still applied for the corresponding fluid or structure elements in the simulation. LS-DYNA adopts the Eulerian algorithm coupled with the Lagrangian formulation to fully model the interaction between the blast wave and the structure. The software package implements a contact interface between the Eulerian and Lagrangian components. Therefore, the interaction between the blast wave and the response of the structure can be captured, even for large deformations [24].

This simulation assumes that there is a large quantity of flammable gas (a mixture of air and acetylene) leaking from storage tanks. In this simulation, we consider flammable gas mixture volumes of $15600\,\text{m}^3$ and $4000\,\text{m}^3$, which are

Table 3: Material parameters of air in numerical simulation.

Material	Density (kg/m^3)	C_0 (Pa)	C_1	C_2	C_3	C_4	C_5	C_6	E_0 (MJ/m^3)	V_0
Atmosphere	1.293	-1.0×10^5	0	0	0	0	0	0	0.25	1.0

Table 4: Material parameters of water in numerical simulation.

Material	Density (kg/m^3)	C (m/s)	S_1	S_2	S_3	γ_0	a	E_0 (MJ/m^3)
Atmosphere	998.2	1647	1.921	−0.096	0	0.35	0	0.0

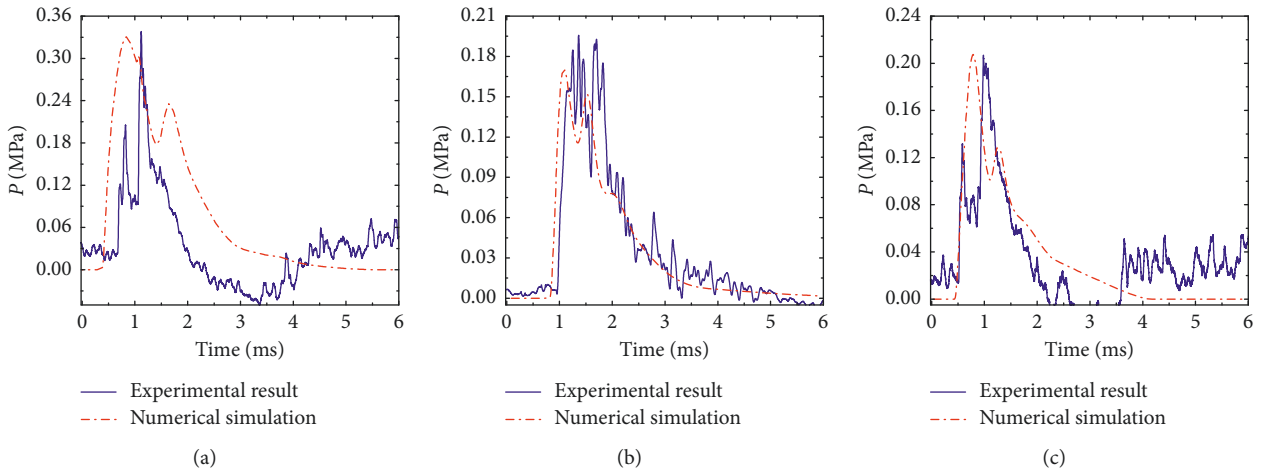

Figure 4: The comparison between experiment and numerical simulation. (a) Gauge A. (b) Gauge B. (c) Gauge D.

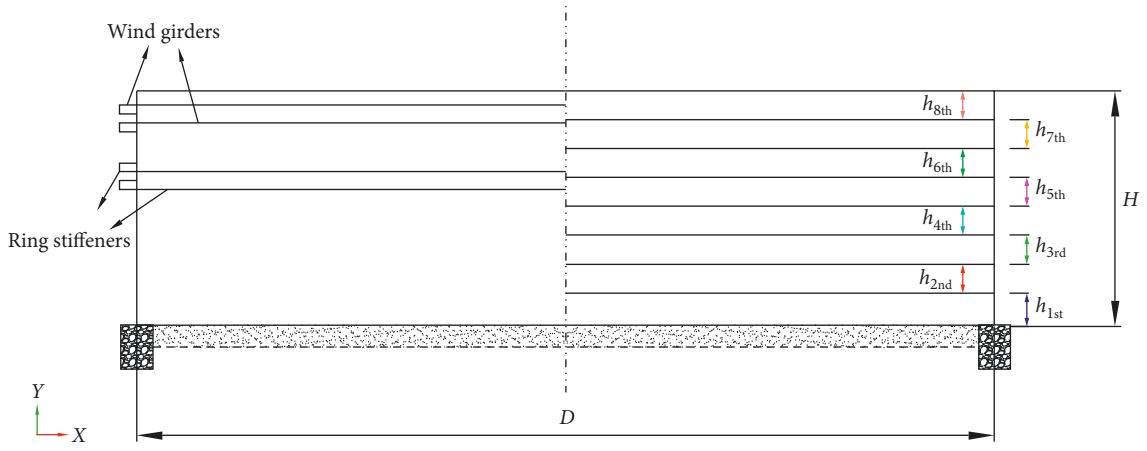

Figure 5: Structure diagram of the storage tank with 15×10^4 m^3 storage capacity.

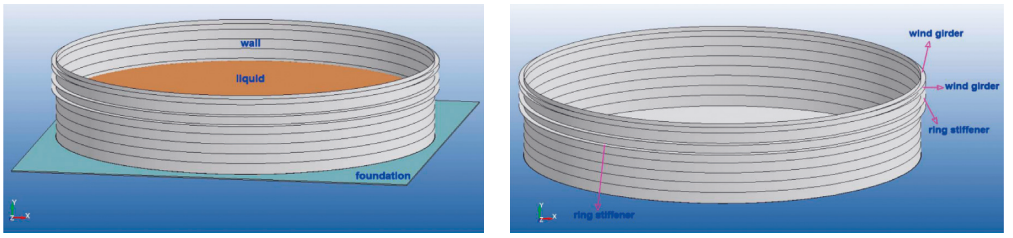

Figure 6: Storage tank and inner liquid. (a) A storage tank with liquid. (b) Wind girders and ring stiffeners.

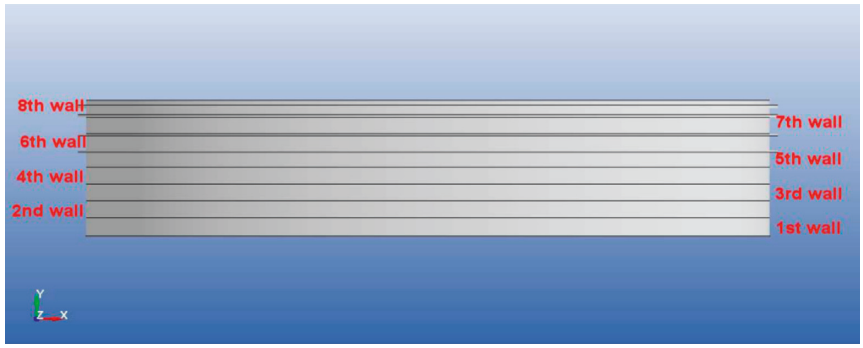

Figure 7: Distribution of eight tank walls.

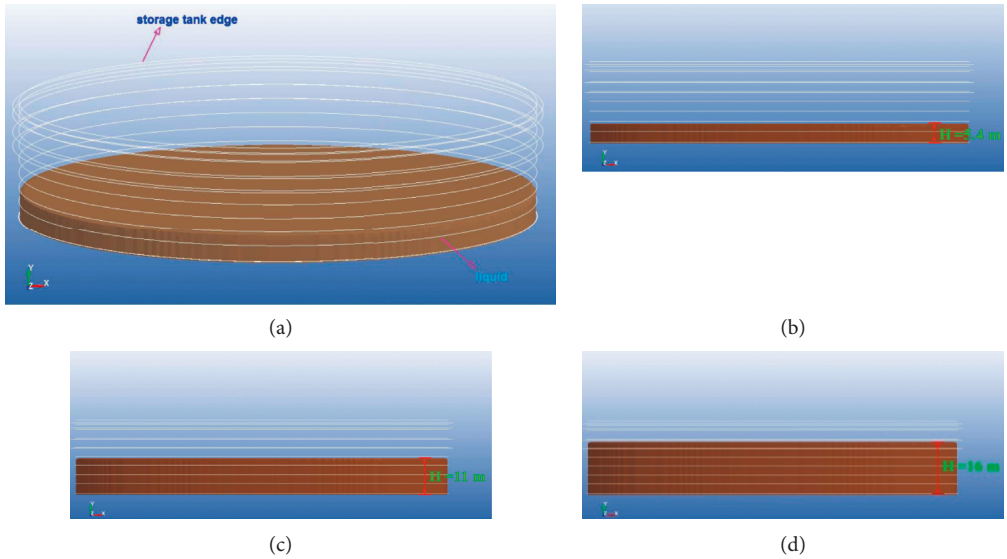

Figure 8: The liquid level conditions. (a) Tank edge and liquid. (b) 25% fill level ($(H)_{\text{liquid}} = 5.4$ meters). (c) 50% fill level ($(H)_{\text{liquid}} = 11$ meters). (d) 75% fill level ($(H)_{\text{liquid}} = 16$ meters).

comparable to the volumes found in some accidents. Compared with the influence of the combustion wave, the impact intensity from the shock wave is much higher, and its damage effect on the storage tank is significantly serious than that of the combustion wave. In the case of the adverse situation in simulations, the shock wave is the main factor in simulating the blast impact loading. The blast wave initiated from the gas mixture and impacted on the storage tank. Figure 9 shows the relative positions of the storage tank and initial explosion. The numerical model of the explosion in this situation follows the model introduced previously.

The TNT equivalency model is based on the assumption of equivalence between the flammable material and TNT. It can be used to evaluate the intensity of gas explosion and the radius of the effect in some explosion accident analysis, such as the multienergy method or TNO method. In addition, the TNT equivalent method presents the similar scaled explosion intensity in different combustible gas volume. Equivalent mass W is calculated (in equation (6)) based on the total heat of combustion of the flammable material [25]:

$$W = \frac{\eta M E_C}{E_{TNT}}, \tag{6}$$

where η is the empirical explosion efficiency, M is the mass of flammable material (equal to the mass of the air and acetylene mixture), E_C is the heat of the reaction of the flammable material, and E_{TNT} is the heat of the TNT reaction. By using equation (1) for the modeled conditions with volumes of 15600 m^3 and 4000 m^3, we found that the blast intensities had TNT equivalent masses of 1500 kg and 380 kg, respectively.

3. Results and Discussion

3.1. Failure Mode Analysis. Figure 10 shows the failure of the tank structure under conditions of different fill levels and blast intensities. With a blast intensity resulting from an explosion of 1500 kg TNT equivalent mass (15600 m^3 gas), Figures 10(a-i), 10(a-ii), and 10(a-iii) show the structural damage with liquid heights of 25%, 50%, and 75%, respectively. Figures 10(b-i), 10(b-ii), and 10(b-iii) show the same fill levels but for the blast intensity of a 380 kg TNT equivalent mass (4000 m^3 combustible gas explosion).

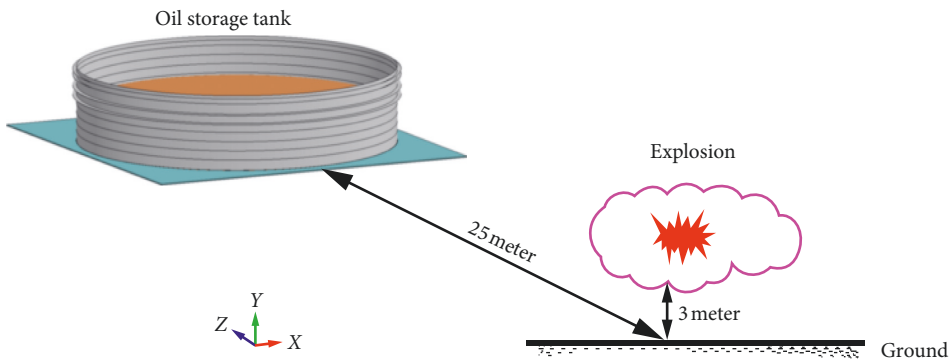

Figure 9: The relative distance between the storage tank and the explosion.

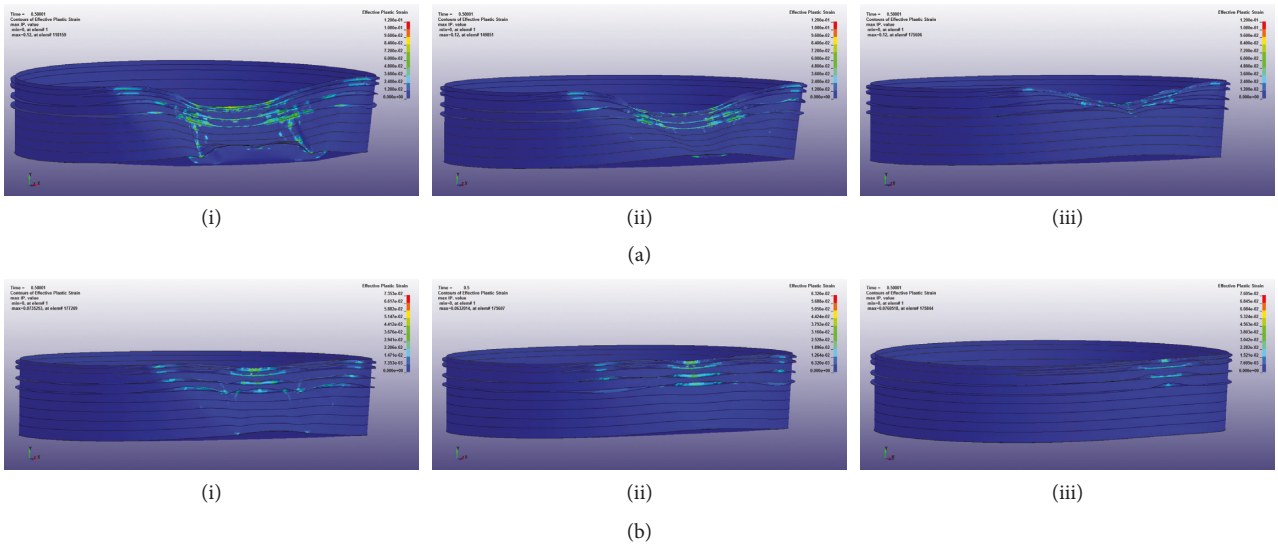

Figure 10: structure damage state in different blast intensity and fill conditions. (a) Under the blast intensity of 1500 kg TNT equivalent mass: (i) 25% fill level; (ii) 50% fill level; (iii) 75% fill level. (b) Under the blast intensity of 380 kg TNT equivalent mass: (i) 25% fill level; (ii) 50% fill level; (iii) 75% fill level.

In general, the tank structures in Figures 10(a-i)–10(a-iii) suffer more significant destruction than those in Figures 10(b-i)–10(b-iii) because of the intensity of the explosion. However, the structural damage is alleviated with increasing fill amounts of oil or liquid fuel when considering the same blast load intensity. For example, the structures in Figures 10(a-i), 10(b-i), 10(a-ii), and 10(b-ii) form clear concave deformations through all walls. Owing to the blast impact, the tank floor and walls (especially walls 1 to 4) are warped and curled up. The structures have an obvious concave deformation, which is distributed almost symmetrically along the stagnation points on the blast side. The buckling deformation of the storage tanks looks like the capital letter "W" at the 25% fill level (in Figures 10(a-i) and 10(b-i)), whereas the deformation of the tanks looks like the capital letter "V" in Figures 10(a-ii) and 10(b-ii), at the 50% fill level.

By contrast, the storage tank experiences less damage with a 75% fill level. Only three tank walls (the sixth through eighth), wind girders, and ring stiffeners are deformed clearly. In this situation, the slight curling in the walls can be observed to look like the lowercase letter "v," as in Figure 10(a-iii), or a blurry letter "o," as in Figure 10(b-iii). In Figure 10(b-iii), the tank body is mostly left intact, except for slight deformation of the wind girders (and ring stiffeners).

3.2. Displacement and Deformation Analysis. To determine displacement δ, a series of measuring points (S_i with $i = 1$–8) are distributed along the storage tank at the midheight of every wall, as shown in Figure 11. The resultant displacements of S_i, at 0.5 s after the detonation, are shown in Figure 12. The resultant displacement is equal to the vector superposition of vertical ($+Y$ axis) and radial ($+Z$ axis) displacement. The displacement of the same point was found to be affected by simulated conditions, namely, the liquid fill level and explosion intensity. In each figure, under the same

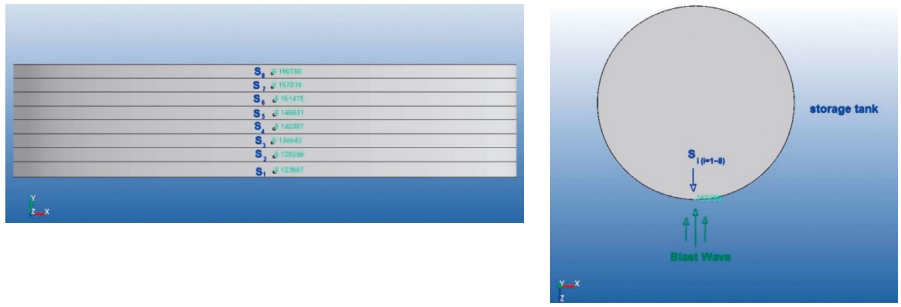

(a) (b)

Figure 11: The distribution of measuring points S_i: (a) front view; (b) top view.

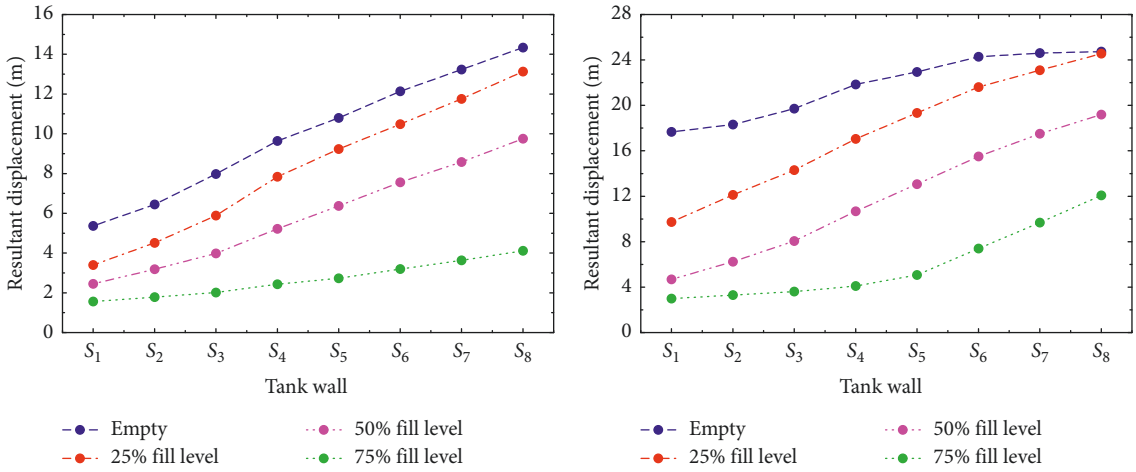

(a) (b)

Figure 12: Resultant displacement of measuring points S_i. (a) Intensity of 380 kg TNT equivalent mass explosion. (b) Intensity of 1500 kg TNT equivalent mass explosion.

blast intensity, deformation displacement δ decreased with increasing liquid fill level. The change in deformation displacement δ in the numerical simulation is consistent with the theoretical analysis.

In order to reveal the influence of constraint conditions on the structure's response under blast loads, we modified the numerical model of the storage tank to include an anchor zone on the bottom plate in the LS-DYNA 3D environment. Additionally, along the circumference of the bottom plate edge, we set the fixed constraints at an interval angle of 5°. Previous numerical results had no constraint on this edge.

Figure 13 shows the storage tank failure state for a blast intensity of a 1500 kg TNT equivalent mass explosion for different fill levels (25% and 50%) with the free (Figures 13(a-i) and 13(b-i)) and fixed (Figures 13(a-ii) and 13(b-ii)) constraint conditions. Compared with the free constraint conditions, the fixed constraint oil storage tanks experience more serious damage. As shown in Figures 13(a-ii) and 13(b-ii), the storage tanks deformed significantly and collapsed severely. Without the constraint condition (Figures 13(a-i) and 13(b-i)), the free bottom plate absorbed part of the blast energy through warping and deformation. Conversely, the fixed plates absorbed hardly any blast energy, meaning more was borne by the tank walls. To reduce blast damage, it is preferable to weaken the constraints on the tank's bottom plate.

Analysis of the resultant displacement and deformation reveals damage to the storage tank under the blast impact in different conditions. A more detailed structural dynamic response can be revealed from an energy analysis and dynamic strain comparison.

3.3. Structural Energy Analysis. In Figures 5 and 6, the storage tank body is composed of eight tank walls and can be divided into many elements, S_i ($i = 1, 2, \ldots, N$). In this section, we analyze the energy variation of shell elements S_i under the blast impact in two tank conditions: empty and liquid filled.

Condition 1 (empty). Suppose blast load $P(t)$ is at the center of shell element S_i and forms deformation displacement δ_1 (as shown in Figures 14(a) and 14(b)). The resistance force to the impact is $D \times \delta_1$, where D is the resistance coefficient of the structure (shell element S_i). Work W_1 is the $P(t)$ working

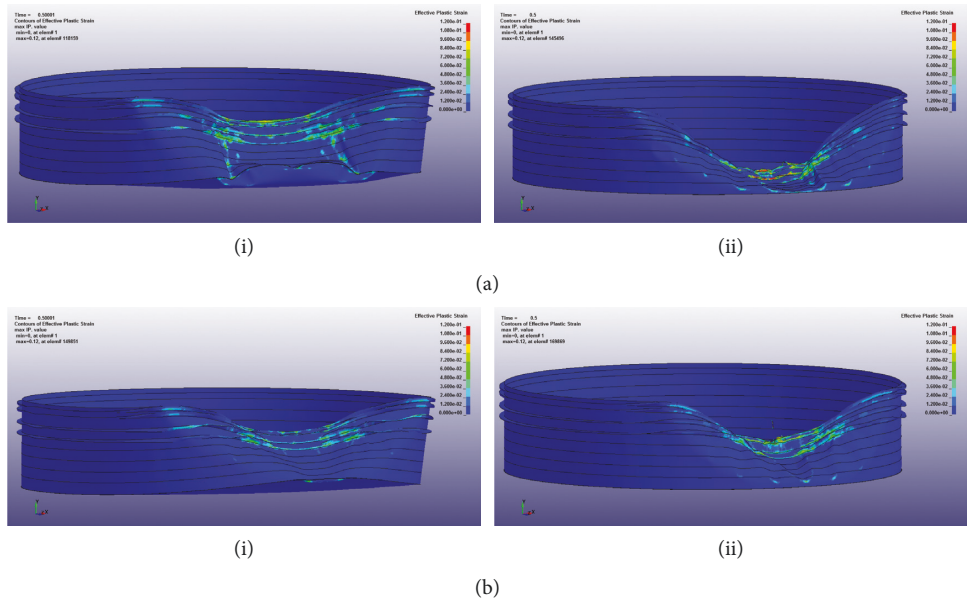

Figure 13: Structural deformation and failure state in different constraint conditions. (a) Storage tank with 25% fill level: (i) no constraint; (ii) fixed constraint. (b) Storage tank with 50% fill level: (i) no constraint; (ii) fixed constraint.

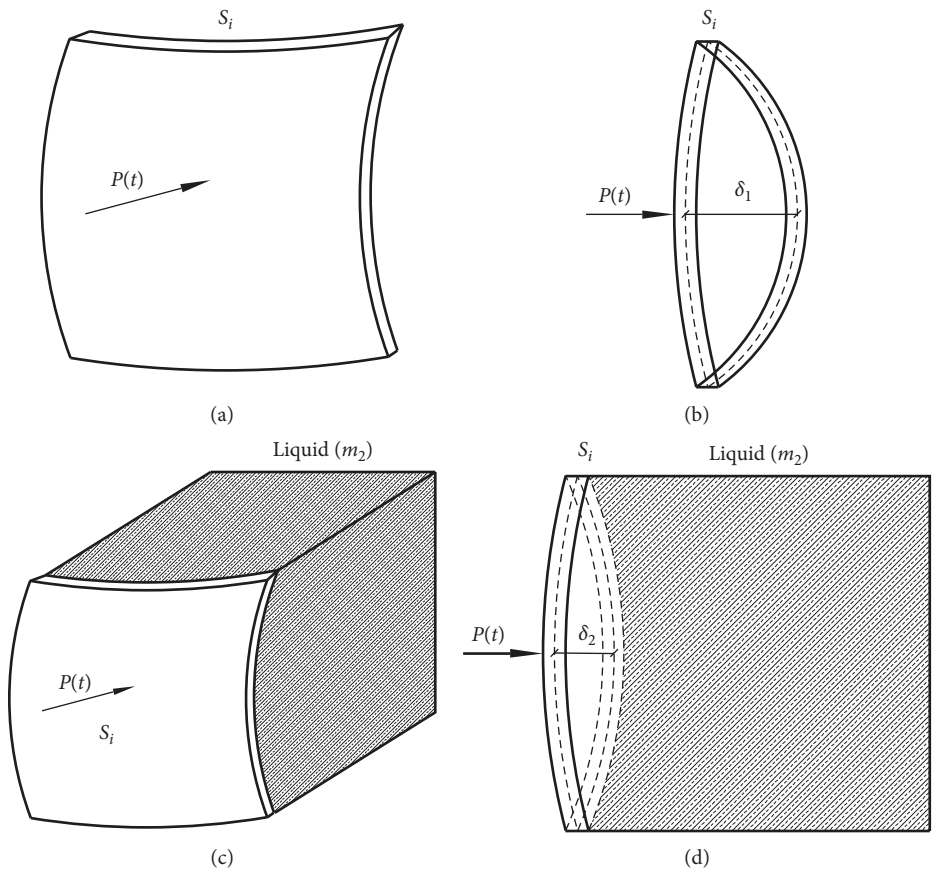

Figure 14: Diagram of shell element S_i in two separate conditions. (a) Shell element in empty condition. (b) Deformation displacement of S_i. (c) Shell element and added liquid mass. (d) Deformation displacement of shell element.

along deformation displacement δ_1. At the moment of blast impact, S_i start to move with velocity $v(t)$. The equations of load and work can be described as follows:

$$P(t) = D \times \delta_1 + m_1 \frac{dv(t)}{dt},$$
$$W_1 = P(t) \times \delta_1. \tag{7}$$

Under the blast impact, after the plastic deformation displacement $\delta_{1\max}$, the velocity and kinetic energy of S_i are almost zero. Ignoring the heat loss during the interaction between the blast wave and the structure, work W_1 is transformed into the element's deformation energy, E_{P1}. The change can be expressed as

$$P(t) \times \delta_{1\cdot\max} = E_{P1}. \tag{8}$$

Condition 2 (liquid filled). When the storage tank is filled with liquid, most shell elements (on the wall) move or vibrate together with the inner liquid, as affected by blast loading $P(t)$. Suppose the mass of shell element S_i and the added liquid are m_1 and m_2. Under the $P(t)$ impact effect, S_i has deformation displacement δ_2 and its resistance to the impact force is $D \times \delta_2$. Similarly to the empty condition, parameters $P(t)$, δ_2, and $v(t)$ have the following relationship:

$$P(t) = D \times \delta_2 + (m_1 + m_2) \frac{dv(t)}{dt}. \tag{9}$$

Under the same intensity $P(t)$, the deformation displacement fulfils the relation $\delta_1 > \delta_2$ in two separate conditions. When the impacted regions of the wall ultimately exhibit plastic deformation, the inner liquid may separate from the structure and continue to shake for a moment. Under the same loading effect, the input energy is changed into two parts—the plastic deformation energy and the kinematic energy of the liquid. The ultimate deformation of shell element S_i is $\delta_{2\cdot\max}$, but the added liquid mass still moves with velocity v_2.

Ignoring heat loss, work W_2 can be transformed into deformation energy E_{P2} and the kinetic energy of liquid, $\mathrm{KE}_{\mathrm{liquid}}$, and can be expressed as follows:

$$P(t) \times \delta_{2\cdot\max} = E_{P2} + \mathrm{KE}_{\mathrm{liquid}} = E_{P2} + \frac{1}{2} m_2 v_2^2,$$
$$E_{P2} = P(t) \times \delta_{2\cdot\max} - \frac{1}{2} m_2 v_2^2. \tag{10}$$

Moreover, blast load $P(t)$ forms an impulse on shell element S_i. According to the theory of impulse, S_i has specific impulse $i(t)$:

$$i(t) = \int_0^t p(t) d\tau. \tag{11}$$

Owing to the momentum during the blast, the velocity of S_i is

$$v_1(t) = \frac{i(t)}{\rho_n h_n}, \tag{12}$$

where ρ_n and h_n represent the material density and thickness of S_i and $\rho_n \times h_n$ represents its unit mass. Assuming that the impact load on S_i is absorbed, it is completely converted into the initial kinetic energy of the shell element when the storage tank is empty. Hence, the absorbing energy expression is given by

$$E_{\mathrm{a}} = \frac{i^2(t)}{2\rho_n h_n} = E_{p1}. \tag{13}$$

In the above equation, E_{a} represents the structural absorption energy that is converted into deformation energy E_{P1}. Alternatively, in the liquid-filled condition, the velocity of S_i with added liquid mass m_2 is

$$v_2(t) = \frac{i(t)}{\rho_n h_n + \rho_0 c_0 t} = \frac{\int_0^t p(t) d\tau}{\rho_n h_n + \rho_0 c_0 t}. \tag{14}$$

In this expression, ρ_0 represents the density of the liquid and c_0 represents the speed of sound in the liquid, while $\rho_0 \times c_0 \times t$ represents the unit mass of the added liquid. Equation (14) also supposes that the impact load on the S_i was absorbed and was completely changed into the initial kinetic energy of shell element S_i and added liquid m_2. Under such conditions, the absorbing energy can be expressed as equations (15) and (16), where E_{P2} represents the deformation energy of shell element S_i:

$$E_{\mathrm{b}} = \frac{i^2(t)}{2(\rho_n h_n + \rho_0 c_0 t)} = E_{P2} + \mathrm{KE}_{\mathrm{liquid}}, \tag{15}$$

$$E_{P2} = \frac{i^2(t)}{2(\rho_n h_n + \rho_0 c_0 t)} - \mathrm{KE}_{\mathrm{liquid}}. \tag{16}$$

Comparison between equations (13) and (15) reveals that if the shell elements move together with the added liquid mass, their deformation energy can be partly reduced compared to the empty condition; that is, $E_{P2} < E_{P1}$.

The tank walls are composed of many shell elements. When empty, E_1 represents the total deformation energy of the tank wall, as

$$E_1 = \sum_{i=1}^{n} E_{P1i}. \tag{17}$$

In the liquid-filled conditions, E_2 represents the total deformation energy of the tank wall:

$$E_2 = \sum_{i=1}^{n} E_{P2i}. \tag{18}$$

The relationship between E_1 and E_2 fulfils the following condition:

$$E_1 > E_2. \tag{19}$$

Under the impact of a 1500 kg TNT equivalent mass explosion, Figure 15 shows time-history curves of the kinetic energy KE and deformation energy E_P of different parts of the tank: the tank walls, wind girders, and bottom plate. The liquid level is the main simulation variable in Figure 13. According to the KE curves, 20–50 ms after detonation, the

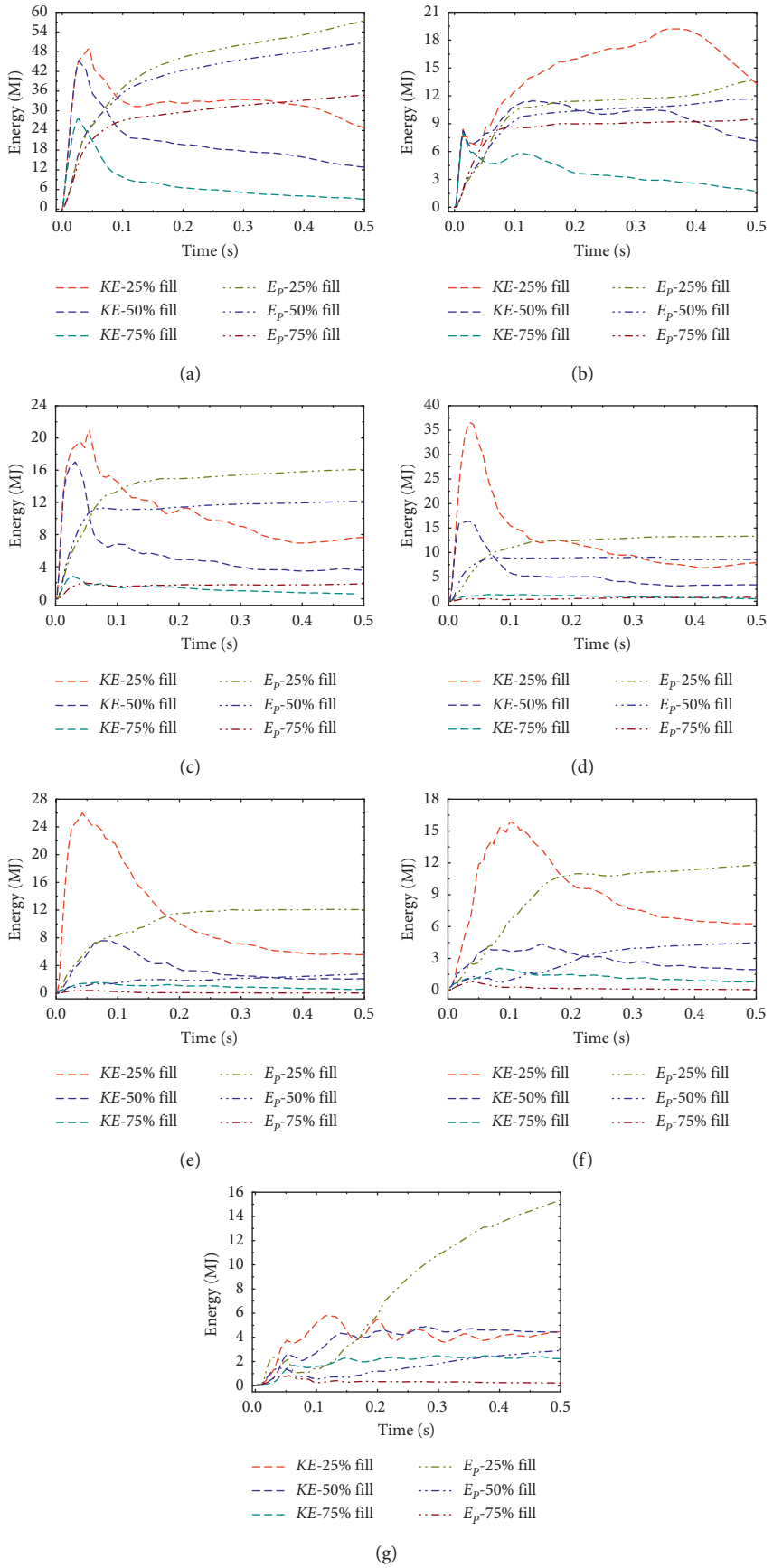

Figure 15: The energy curves comparison under intensity of 1500 kg TNT equivalent mass explosion. (a) Wind girders (ring stiffeners). (b) 8th wall. (c) 6th wall. (d) 5th wall. (e) 3rd wall. (f) 1st wall. (g) Bottom plate.

wind girders and most tank walls reach their maximum energy value. In contrast, most structure parts form visible residue energy on their E_P curves after 0.5 s. The energy variation in the KE and E_P curves reveals that the blast energy is absorbed by structures and is converted into deformation energy.

Furthermore, Tables 5 and 6 list the collected E_P data of the different tank parts at the simulation termination. Table 5 compares the data for different liquid levels in storage tanks with no constraints, whereas Table 6 shows the energy data for fixed constraint conditions. Tables 5 and 6, as well as Figure 15, reveal the following structural energy and failure features of the storage tank structure:

(1) Compared with other parts of the storage tank, the energy values of the wind girders are noticeably higher. The deformed wind girders absorb 35–65% of total deformation energy. These girders are always designed to have a thin-walled rectangular shape and cantilever structures. They are designed to enhance the lateral stiffness of the storage tank and resist the lateral load of wind. As they are not designed considering blast impact effects, the wind girders, with their cantilever shape, are apt to be destroyed.

(2) Under the blast impact, the tank walls stored some energy in structures via deformation. Followed by increases in the inner liquid (from the 25% to 75% fill level), the declining tendency of deformation energy is notable. At the 25% and 50% fill levels, the most energy was absorbed by the sixth wall; at the 75% fill level, the eighth wall absorbed the most energy. The same trend occurs in Tables 5 and 6 (highlighted in bold). For further analysis of the energy variation for tank walls, we undertake a detailed quantitative comparison of the energy feature analysis in next paragraphs, with consideration of liquid levels, constraint conditions, and blast load intensity.

(3) As shown in Figure 14, the bottom plate with no constraints warps and distorts under the blast wave. Table 5 compares the deformation energy of the bottom plate for different liquid levels. At the 25% fill level, the bottom plate forms 15.35 MJ energy, which accounts for 9.3% of the total energy. When the inner liquid rises to the 50% fill level, the value significantly declines to 2.9 MJ and only accounts for 2.8% of the total energy. The energy becomes the lowest at the 75% fill level, where it is 0.22 MJ, which is less than 0.5% of the total energy. In Table 6, for all liquid levels, the deformation energy of bottom plate is zero because of the fixed constraint condition applied to these simulations. Regardless of constraint condition, most energy is absorbed by tank walls and other structures.

To analyze the energy features, we compared the energy data of five typical tank walls—the first, third, fifth, sixth, and eighth. The parameters KE_{max} and E_{PT} are used to represent the peak value in the KE curve and the E_P curve at the termination time (0.5 s) respectively, as shown in Figure 16. Figure 17 shows a comparison of these two parameters in different simulation conditions and describes the variation in structural energy quantitatively.

In Figures 17(a-i) and 17(b-i), the KE_{max} parameter curves increase gradually from the first to the fifth tank walls for the 25% and 50% fill level conditions. The curves peak at the fifth or sixth wall. In the 75% fill level condition, KE_{max} grows by a small amount from the first wall to the sixth wall but increases dramatically at the eighth wall. Compared with the fixed constraint model, the KE_{max} value of the free constraint model is larger (especially at the first and third walls). The influence of the fixed bottom plate restricts the movement of the tank walls and reduces to the kinetic energy. The KE_{max} comparison shows that the storage tank walls produce a similar response (in the free and fixed constraint conditions) during the initial impact phase. This initial dynamic response might be closely related to the structural style of the thin-walled cylindrical shell.

The fixed constraint model leads to higher values of parameter E_{PT} than the free constraint model, especially at the 25% and 50% fill levels. In the fixed model, the bottom plate absorbs almost no energy from the blast wave. In the free constraint model, the free bottom plate dissipates the blast energy through deformation and sliding friction, which reduces the energy that the remaining walls and structure must absorb.

The bar charts in Figure 18 compare the total values of E_{PT} for structures with different liquid levels. Here, the deformation energy of an empty storage tank was also calculated. In Figure 18, increasing fill levels clearly reduce the deformation energy. This reduction is found for both conditions of constraint and blast intensities.

For instance, in the 1500 kg TNT equivalent mass explosion condition, the fixed and free constraint models at the 75% fill level have only 21.8% and 17.2% of the deformation energy of the empty tank, respectively. At the 380 kg TNT equivalent mass explosion intensity, a similar trend in deformation energy was observed. As shown in Figure 18(b), at a fill level of 75%, the fixed and the free constraint values observed were only 6.13% and 6.9% of the deformation energy of an empty tank for the respective constraint conditions. Comparing the E_{PT} of the fixed and free constraint models, Figure 18(b) shows that the free constraint condition reduces the impact effect on the tank structures.

The results in Figure 18 indicate that the inner liquid absorbs part of the energy from the blast wave. It reduces the impact of the blast on the storage tanks and the deformation energy.

3.4. Dynamic Strain Analysis. Figure 19 shows several measurement gauges A_i ($i = 1, 2, \ldots, 8$) that represent related shell elements S_i, which are located on each tank wall. The following sections compare the effective strain curves of gauges A_i under the blast intensity of a 1500 kg TNT equivalent mass explosion.

If the lengths of shell element S_i are dS_α, dS_β, and dZ, the volume of S_i fulfils the following relation:

Table 5: Deformation energy of storage tank with no constraint (unit: MJ).

Structure	25% filled (H_{liquid} = 5.4 m)		50% filled (H_{liquid} = 11 m)		75% filled (H_{liquid} = 16 m)	
	Deformation energy (E_{PT})	Percentage	Deformation energy (E_{PT})	Percentage	Deformation energy (E_{PT})	Percentage
Bottom plate	15.35	9.3	2.9	2.8	0.22	0.41
1st wall	11.8	7.2	4.48	4.3	0.07	0.13
2nd wall	8.45	5.1	1.45	1.4	0.03	0.06
3rd wall	12.08	7.3	2.81	2.7	0.03	0.05
4th wall	8.22	5	1.57	1.5	0.13	0.25
5th wall	13.32	8.1	8.57	8.1	0.84	1.6
6th wall	**16.09**	**9.7**	**12.13**	**11.5**	1.88	3.4
7th wall	8.52	5.2	9	8.5	7.09	13
8th wall	13.70	8.3	11.63	11	**9.51**	**17.4**
Wind girders	57.4	34.8	50.78	48.2	34.78	63.7
Total energy	164.93		105.33		54.6	

Table 6: Deformation energy of oil storage tank with fixed constraint (unit: MJ).

Structure	25% filled (H_{liquid} = 5.4 m)		50% filled (H_{liquid} = 11 m)		75% filled (H_{liquid} = 16 m)	
	Deformation energy (E_{PT})	Percentage	Deformation energy (E_{PT})	Percentage	Deformation energy (E_{PT})	Percentage
Bottom plate	0	0	0	0	0	0
1st wall	23.68	12.3	9.41	7	0.14	0.18
2nd wall	8.14	4.2	5.21	3.9	0.93	1.2
3rd wall	11.07	5.8	2.98	2.2	0.76	0.99
4th wall	9.84	5.1	4.61	3.4	0.89	1.2
5th wall	15.5	8.1	10.54	7.9	2.17	2.8
6th wall	**24.16**	**12.6**	**16.27**	**12.1**	4.7	6.1
7th wall	13.75	7.2	12.55	9.4	10.06	13.1
8th wall	19.39	10.1	16.11	12	**18.92**	**24.6**
Wind girders	66.33	34.6	56.44	42.1	38.37	49.9
Total energy	191.85		134.22		76.95	

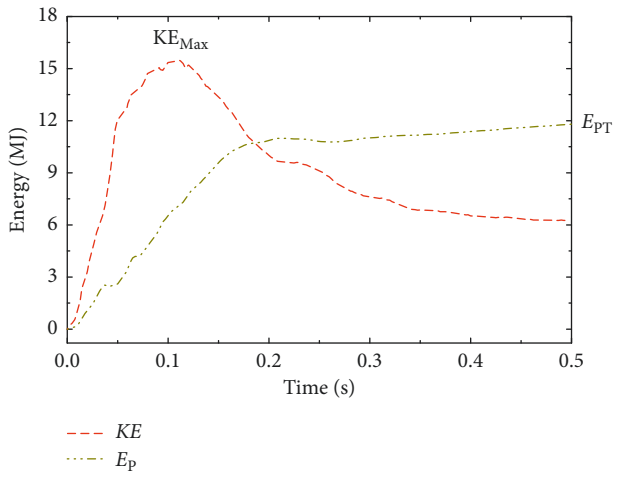

Figure 16: Schematic of energy feature parameters.

$$dV = dS_\alpha \cdot dS_\beta \cdot dZ = AB\left(1 + \frac{z}{R_1}\right)\left(1 + \frac{z}{R_2}\right)d\alpha\, d\beta\, dZ. \tag{20}$$

In equation (20), A and R_1 represent the Lame coefficient and radius of curvature in the α direction in the curvilinear coordinates in Figure 20; B and R_2 denote the Lame coefficient and radius of curvature in the β direction in the same curvilinear coordinates; and z indicates the distance between the external (or internal) surface and the middle surface. Therefore, the deformation energy of shell element E_P can be expressed as

$$dE_p = \frac{1}{2}\left(\sigma_\alpha^z \varepsilon_\alpha^z + \sigma_\beta^z \varepsilon_\beta^z + \sigma_Z^z \varepsilon_Z^z + \tau_{\alpha\beta}^z \gamma_{\alpha\beta}^z + \tau_{\alpha Z}^z \gamma_{\alpha Z}^z + \tau_{\beta Z}^z \gamma_{\beta Z}^z\right) \cdot \left(1 + \frac{z}{R_1}\right)\left(1 + \frac{z}{R_2}\right)AB\, d\alpha\, d\beta\, dZ, \tag{21}$$

where $\sigma_\alpha^z, \sigma_\beta^z, \sigma_Z^z, \tau_{\alpha\beta}^z, \tau_{\alpha Z}^z$, and $\tau_{\beta Z}^z$ are the normal and shear stresses along the α, β, and Z axes on the external surface of S_i and $\varepsilon_\alpha^z, \varepsilon_\beta^z, \varepsilon_Z^z, \gamma_{\alpha\beta}^z, \gamma_{\alpha Z}^z$, and $\gamma_{\beta Z}^z$ denote the normal and shear strains in the α, β, and Z directions on the external surface of S_i.

The theory of thin-shelled structure includes two basic assumptions:

(1) $\gamma_{\alpha z} = 0, \gamma_{\beta z} = 0$.

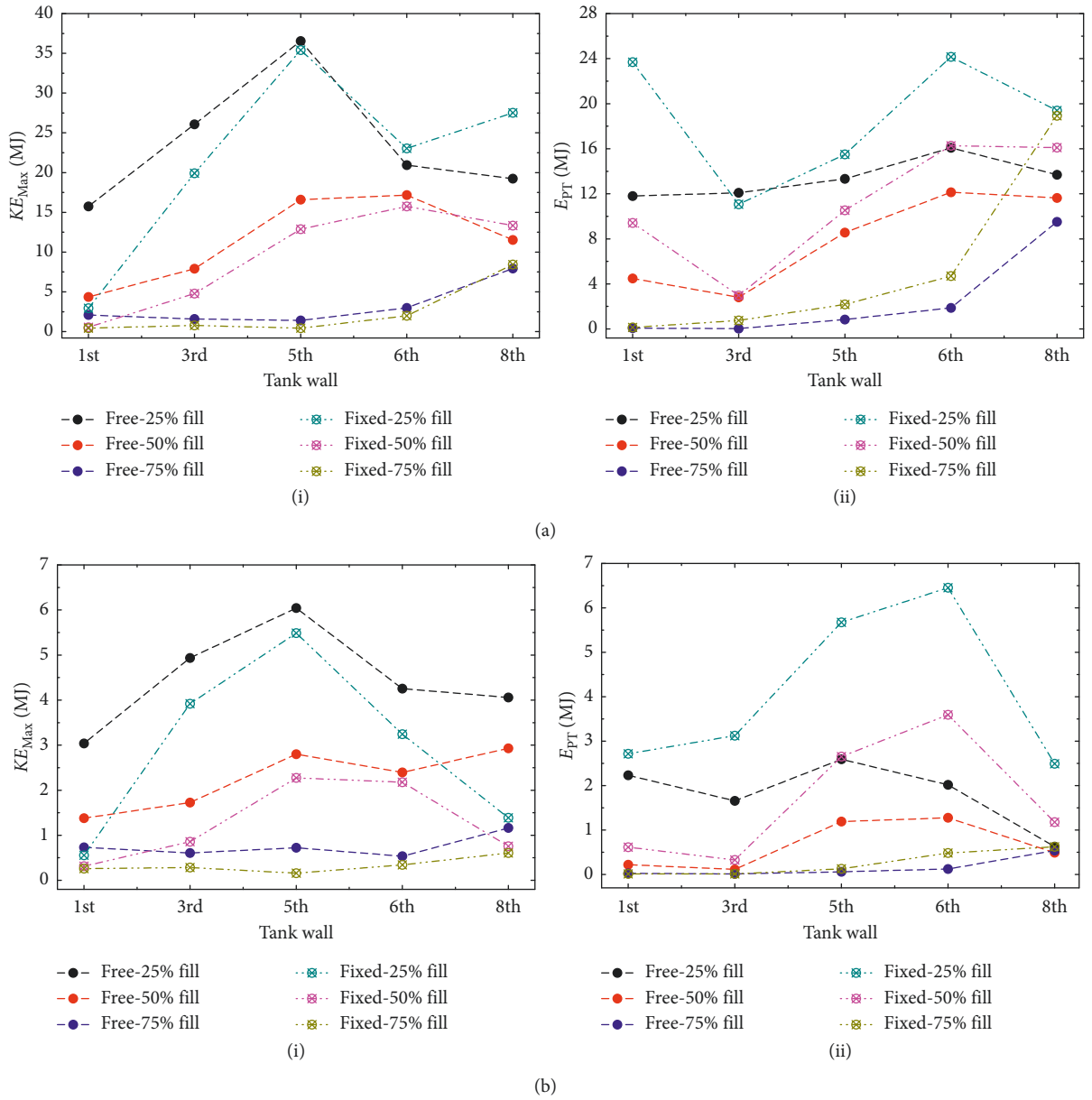

FIGURE 17: Comparisons of energy parameters under different intensities. (a) Intensity of 1500 kg TNT equivalent mass explosion: (i) KE_{max}; (ii) EPT. (b) Intensity of 380 kg TNT equivalent mass explosion: (i) KE_{max}; (ii) EPT.

(2) $\sigma_z \approx 0$.

Equation (22) can therefore be expressed as

$$E_p = \frac{1}{2}\iiint\left(\sigma_\alpha^z\varepsilon_\alpha^z + \sigma_\beta^z\varepsilon_\beta^z + \tau_{\alpha\beta}^z\gamma_{\alpha\beta}^z\right) \cdot \left(1+\frac{z}{R_1}\right)\left(1+\frac{z}{R_2}\right)AB\,d\alpha\,d\beta\,dZ. \tag{22}$$

Equation (23) shows Hooke's law:

$$\begin{cases} \sigma_\alpha^z = \dfrac{E}{1-\mu^2}\left(\varepsilon_\alpha^z + \mu\varepsilon_\beta^z\right), \\ \sigma_\beta^z = \dfrac{E}{1-\mu^2}\left(\varepsilon_\beta^z + \mu\varepsilon_\alpha^z\right), \\ \tau_{\alpha\beta}^z = \dfrac{E}{2(1+\mu)}\gamma_{\alpha\beta}^z. \end{cases} \tag{23}$$

Equation (24) fulfils the geometrical relationships in a thin-walled cylindrical shell structure:

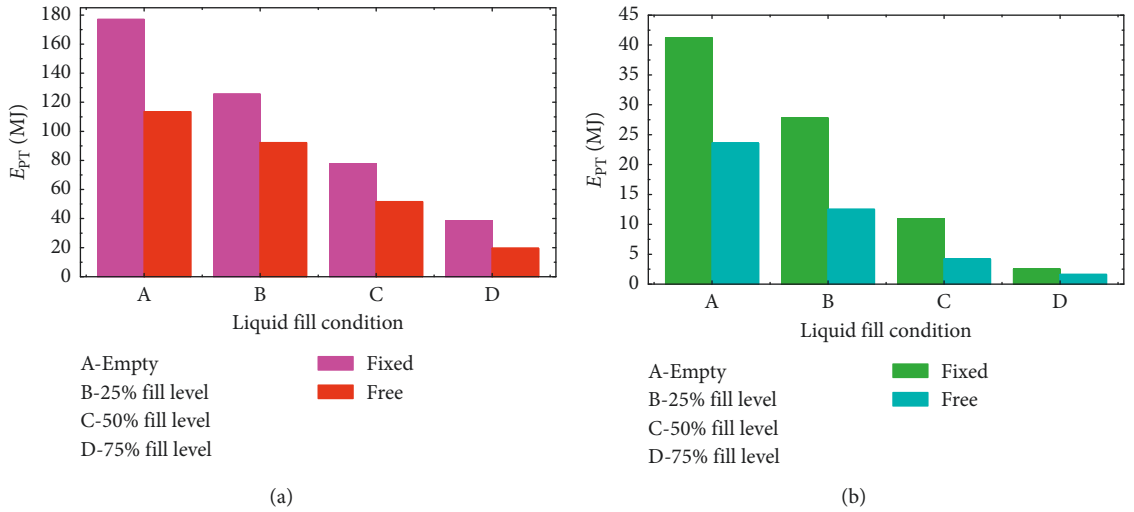

Figure 18: Comparisons of deformation energy $(E)_{PT}$ in different simulation conditions. (a) Intensity of 1500 kg TNT equivalent mass explosion. (b) Intensity of 380 kg TNT equivalent mass explosion.

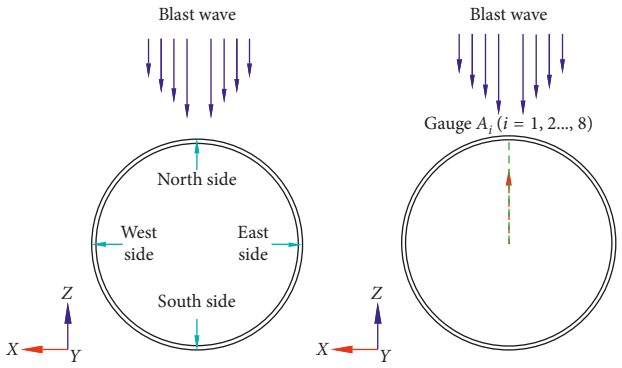

Figure 19: Layout of strain measuring gauges.

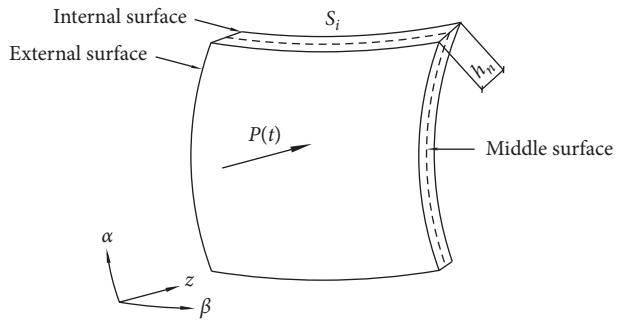

Figure 20: Shell element in curvilinear coordinates α, β, and z.

$$\begin{cases} 1 + \dfrac{z}{R_1} = 1, \\ 1 + \dfrac{z}{R_2} \approx 1, \\ A = B = 1. \end{cases} \tag{24}$$

Additionally, the shell element strain fulfils the following conditions [26]:

$$\begin{cases} \varepsilon_\alpha = \dfrac{\partial v}{\partial \alpha} + \dfrac{1}{2}\left(\dfrac{\partial w}{\partial \alpha}\right)^2, \\ \varepsilon_\beta = \dfrac{\partial u}{\partial \beta} + \dfrac{w}{R}\dfrac{1}{2}\left(\dfrac{\partial w}{\partial \alpha}\right)^2, \\ A = B = 1. \end{cases} \tag{25}$$

$$\begin{cases} \chi_\alpha = -\dfrac{\partial^2 w}{\partial \alpha^2}, \\ \chi_\beta = -\dfrac{\partial^2 w}{\partial \beta^2}, \\ \chi_{\alpha\beta} = -\dfrac{\partial^2 w}{\partial \beta \partial \alpha}. \end{cases} \tag{26}$$

$$\begin{cases} \varepsilon_\alpha^z = \varepsilon_\alpha + \chi_\alpha z, \\ \varepsilon_\beta^z = \varepsilon_\beta + \chi_\beta z, \\ \varepsilon_{\alpha\beta}^z = \gamma_{\alpha\beta} + \chi_{\alpha\beta} z. \end{cases} \tag{27}$$

where ε_α, ε_β, and $\gamma_{\alpha\beta}$ represent the normal and shear strains along the α and β axes on the middle surface of shell element S_i; χ_α, χ_β, and $\chi_{\alpha\beta}$ denote curvature and torsion variation in the α and β directions on the middle surface; and v, u, and w represent the deformation displacement along the α, β, and Z axes on the middle surface.

Equation (22) can satisfy the relations in equations (23)–(27). The final expression of deformation energy is derived as shown in the following equation:

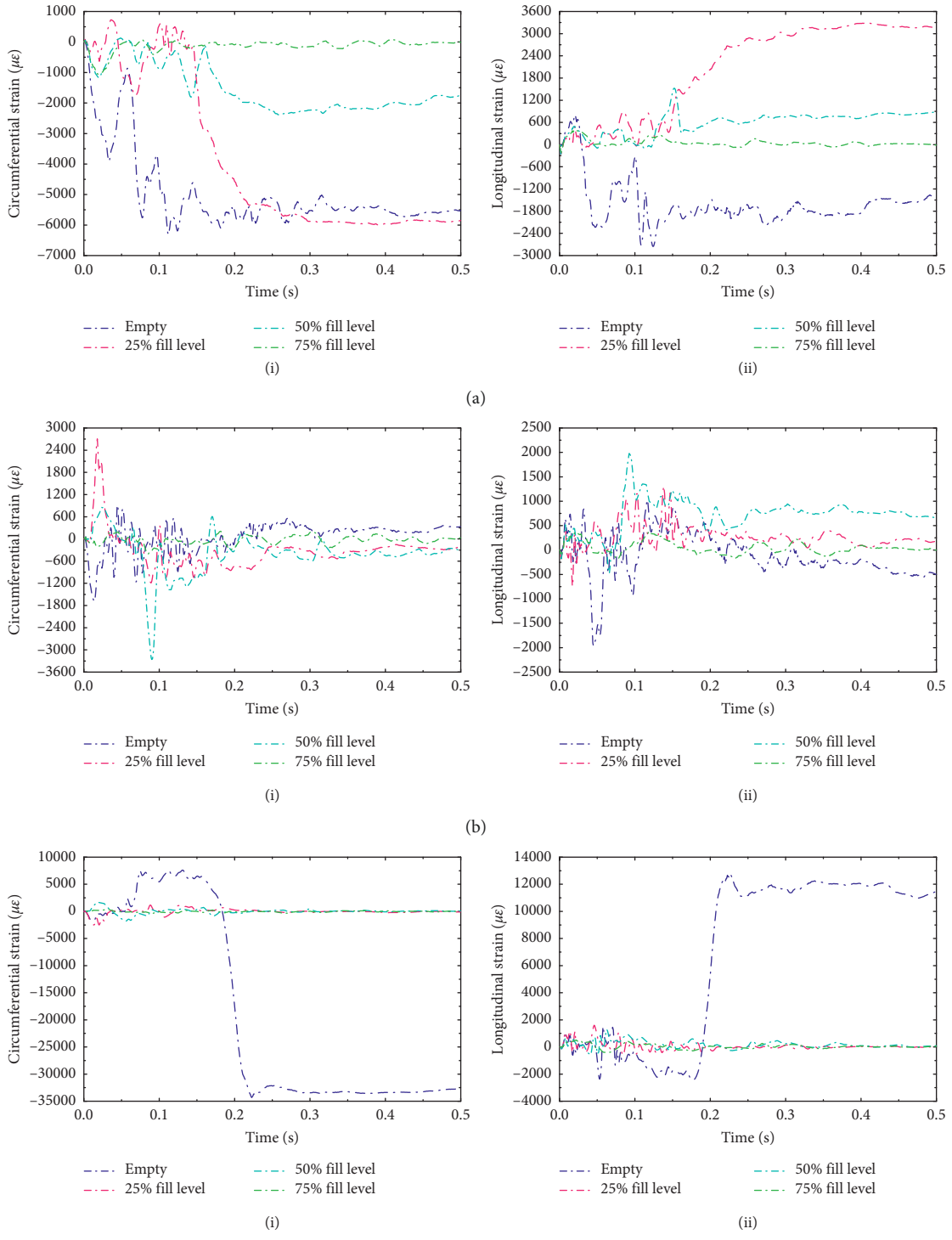

Figure 21: Continued.

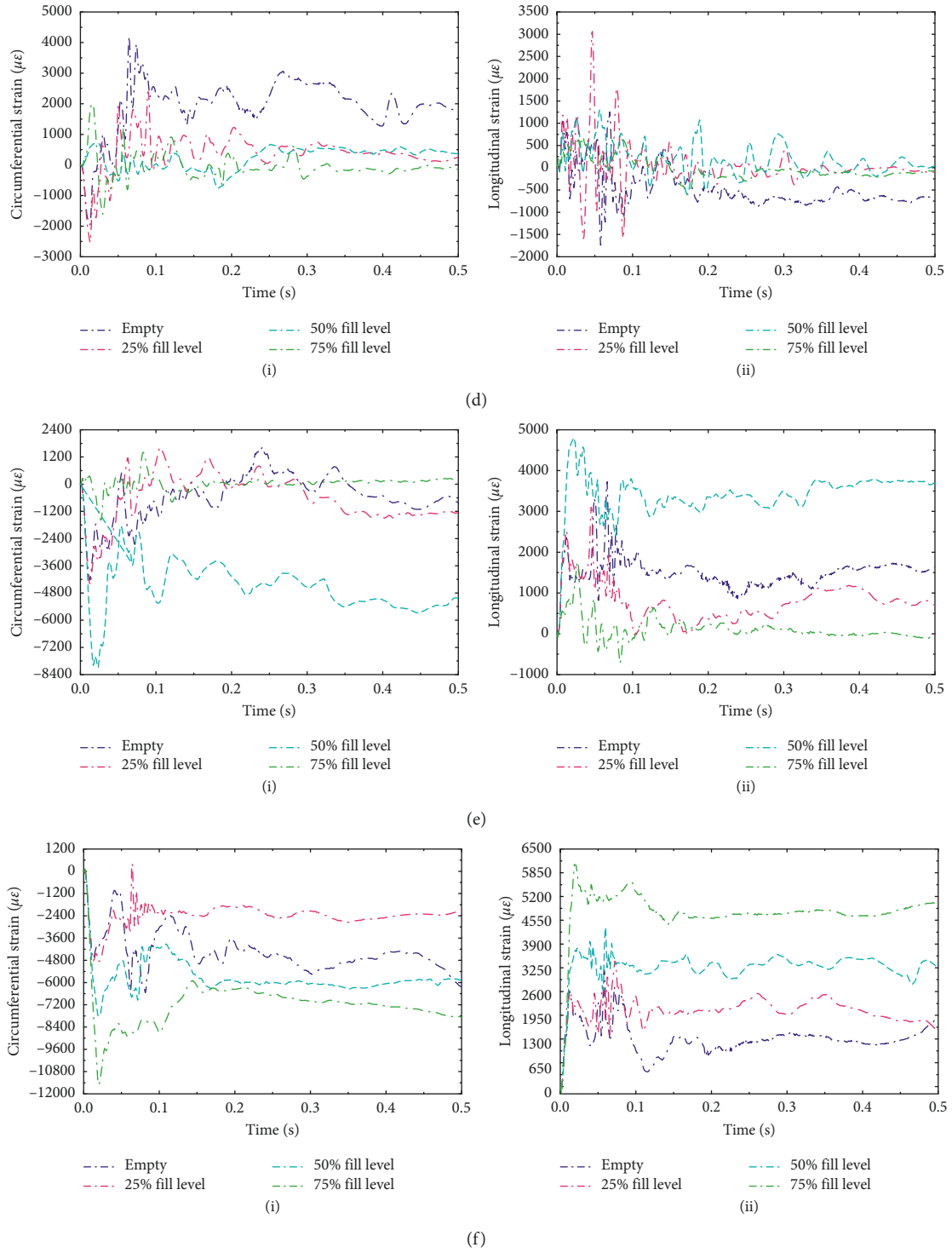

Figure 21: Comparison of circumferential strain and longitudinal strain. (a) 1st wall: (i) circumferential strain; (ii) longitudinal strain. (b) 2nd wall: (i) circumferential strain; (ii) longitudinal strain. (c) 3rd wall: (i) circumferential strain; (ii) longitudinal strain. (d) 4th wall: (i) circumferential strain; (ii) longitudinal strain. (e) 6th wall: (i) circumferential strain; (ii) longitudinal strain. (f) 7th wall: (i) circumferential strain; (ii) longitudinal strain.

$$\begin{cases} E_p = U_1 + U_2, \\ U_1 = \dfrac{Eh_n}{2(1-\mu^2)} \iint_A \left[\left(\varepsilon_\alpha + \varepsilon_\beta\right)^2 - 2(1-\mu)\left(\varepsilon_\alpha \varepsilon_\beta - \dfrac{1}{4}\gamma_{\alpha\beta}^2\right)\right] d\alpha\, d\beta, U_2 = \dfrac{D}{2} \iint_A \left[\left(\chi_\alpha + \chi_\beta\right)^2 - 2(1-\mu)\left(\chi_\alpha \chi_\beta - \chi_{\alpha\beta}^2\right)\right] d\alpha\, d\beta. \end{cases} \tag{28}$$

Equation (28) reveals that deformation energy E_P comprises U_1 and U_2. U_1 is the strain energy of shell element S_i along the direction of thickness (the direction of blast load $P(t)$) and represents the strain energy of the shell element in the membrane stress state, whereas U_2 includes the curvature and torsion variation parameters of middle surfaces χ_α, χ_β, and $\chi_{\alpha\beta}$, thus representing the bending strain energy. As stated in the above expressions, there is a relationship between deformation energy E_P and the dynamic strain of the corresponding shell structures. That is, the structural variation feature in energy analysis can be reflected in changes in dynamic strain. As depicted in Figure 15 and Table 5, as the inner liquid fill level rises (from 25% to 75%), there is a significant decrease in the deformation energy of some tank walls. For example, at the 25% and 50% fill levels, the deformation energy in the sixth wall is much greater than in other parts of the tank, though its energy sharply decreases at the 75% fill level. Similar changes in deformation energy can be reflected in the structural strain energy of the middle surface (especially reflected in the circumferential or longitudinal strain of the shell element). In the following section, we compare the dynamic variation in the shell's circumferential or longitudinal strain (A_i in Figure 19) for different fill conditions.

3.5. Strain Comparison. Figure 21 depicts the detailed circumferential strain (along the β axis in Figure 20) and longitudinal strain (along the α axis in Figure 20) curves of Gauge A on the walls of the storage tank (shown in Figure 19 as Gauge A_i). Figure 21(a) compares the strain readings on the first wall at different liquid levels. Under the blast impact, the first tank wall experiences noticeable compression (along the β axis) when empty or 25% full. The longitudinal stress state (along the α axis) at these fill levels is quite different. The effect of compressive and tensile stresses on structures is greatly reduced as the fill level increases. For example, at the 25% fill level, the residual of the circumferential and longitudinal strains are −5855 με and 3164 με, respectively. In contrast, at the 75% fill level, these strain values decrease sharply, $-7\,\mu\varepsilon$ and $11\,\mu\varepsilon$, respectively. The fill level conditions seem to have minimal effect on the strain of the second tank wall, as shown in Figure 21(b).

As described in the previous section, the tank floor and some walls—especially the first, second, and third walls—are significantly influenced by the blast impact, which causes them to warp and curl. If the height of the inner fuel liquid is greater than 11 m, the dynamic strain of the first wall is effectively relieved. However, the liquid fill has little influence on the strain curves of the second wall.

Changes in the fuel liquid level also significantly influence the third through fifth walls. As shown in Figure 21(c), the curves of the empty tank walls have obvious negative values along the circumferential direction and positive values along the longitudinal direction, indicating that the corresponding shell structure bears compression along the circumferential direction and tension along the longitudinal direction. In contrast, in other liquid fill conditions, the curves of the third tank wall exhibit clear oscillations near the initial strain (i.e., $0\,\mu\varepsilon$). Through this oscillation, the structure experiences elastic compression and tension. The dynamic strain reveals further differences between the empty and fuel-filled conditions on the fourth and fifth walls (for example, as shown in Figure 21(d)).

In Figure 21(e), a clear change is shown at the 50% fill level: the strain on the sixth wall increases sharply compared to other conditions when shell structure S_i lies above the inner liquid (at the 50% fill level). Compared to the empty and 25% fill level conditions, the dynamic strain at the same place is weaker. By contrast, the 75% liquid fill condition has a curve with an oscillation near the initial value under the blast impact because the related shell structure S_i still lies under the inner liquid.

When shell element S_i is higher than the inner liquid, such as on the seventh wall (shown in Figure 21(f)) or on the eighth wall, the dynamic strain of related shell structures bears limited influence on the inner liquid. For example, when comparing the circumferential and longitudinal strain curves between the empty and fuel-filled conditions, it is difficult to find the rule underlying the change in Figure 21(f). However, the strain curves in Figure 21 show that most shell structures on the north sides of walls form compressive stress along the circumferential direction and tensile stress along the longitudinal direction, owing to the storage tank buckling deformation that occurs under the blast wave impact on the north side of the walls.

4. Conclusions

In this paper, we have described the dynamic response of and damage to a simplified storage tank prototype with a capacity of $15 \times 10^4\ \mathrm{m}^3$. First, we introduced an experimental scale-model explosion test, the results of which were then used to validate numerical models that provide a tool for extensive assessment. Subsequently, the numerical models were employed to examine storage tanks with different conditions. Their dynamic response was simulated in nonlinear FE software, LS-DYNA. The key findings can be summarized as follows:

(1) When considering the effect of constraint conditions, fixed tanks deform significantly and collapse more easily because a free bottom plate absorbs part of the blast energy through warping and

deformation, whereas a fixed base plate absorbs little energy. Hence, to reduce blast impacts, it is preferable to weaken constraints on the tank's bottom plate.

(2) Over time, the walls form energy in the process of deformation under the blast impact. This deformation energy decreases with increases in the inner liquid level (from 25% to 75%).

(3) Combined with theoretical analysis, the previous result demonstrates that liquid may absorb energy from the blast wave. Liquid can reduce the structural deformation energy and the effect of blast loading on a storage tank. Thus, increasing the level of fuel liquid in storage tanks can play a positive role in relieving the impact of a blast wave.

(4) Owing to their thin-walled rectangular shape and cantilever structural style (designed for resisting lateral loads from wind), wind girders (ring stiffeners) are prone to damage from blast impacts. Compared with other structures, wind girders are more seriously damaged and form more deformation energy.

(5) Theoretical analysis of shell element deformation energy E_P shows that it is composed of two parts: strain energy U_1 and bending strain energy U_2. Therefore, if E_P is changed in simulation conditions, similar changes are reflected in the structural strain energy of the middle surface (especially in the circumferential or longitudinal strain of the shell element).

Data Availability

The data used to support the findings of this study are available from the corresponding author upon request.

Conflicts of Interest

The authors declare that they have no conflicts of interest.

Acknowledgments

The authors gratefully acknowledge the financial support of the National Natural Science Foundation of China (grant no. 51508123) (The floating-roof oil tank structure dynamic response under blast loading based on material point method); Blast-Resistant Capacity and Defense Strategies of Spatial Latticed Structures Based on FRP-Steel Seismic Reduction Members (grant no. 51708521); Fundamental Research Funds for the Central Universities (grant no. HEUCFM160202); and State Scholarship Fund of China (grant no.201806685031).

References

[1] D. Wang, P. Zhang, and L. Chen, "Fuzzy fault tree analysis for fire and explosion of crude oil tanks," *Journal of Loss Prevention in the Process Industries*, vol. 26, no. 6, pp. 1390–1398, 2013.

[2] L. Shi, J. Shuai, and K. Xu, "Fuzzy fault tree assessment based on improved AHP for fire and explosion accidents for steel oil storage tanks," *Journal of Hazardous Materials*, vol. 278, pp. 529–538, 2014.

[3] M. S. Mannan, *Lees' Loss Prevention in the Process Industries-Hazard Identification, Assessment and Control*, Cambridge, UK, 4th edition, 2012.

[4] C. D. Argyropoulos, M. N. Christolis, Z. Nivolianitou, and N. C. Markatos, "A hazards assessment methodology for large liquid hydrocarbon fuel tanks," *Journal of Loss Prevention in the Process Industries*, vol. 25, no. 2, pp. 329–335, 2012.

[5] J. I. Chang and C.-C. Lin, "A study of storage tank accidents," *Journal of Loss Prevention in the Process Industries*, vol. 19, no. 1, pp. 51–59, 2006.

[6] D. Wu and Z. Chen, "Quantitative risk assessment of fire accidents of large-scale oil tanks triggered by lightning," *Engineering Failure Analysis*, vol. 63, pp. 172–181, 2016.

[7] M. Djermane, D. Zaoui, B. Labbaci, and F. Hammadi, "Dynamic buckling of steel tanks under seismic excitation: numerical evaluation of code provisions," *Engineering Structures*, vol. 70, pp. 181–196, 2014.

[8] L. Yang, Z. Chen, G. Cao, C. Yu, and W. Guo, "An analytical formula for elastic-plastic instability of large oil storage tanks," *International Journal of Pressure Vessels and Piping*, vol. 101, pp. 72–80, 2013.

[9] F. Berahman and F. Behnamfar, "Probabilistic seismic demand model and fragility estimates for critical failure modes of un-anchored steel storage tanks in petroleum complexes," *Probabilistic Engineering Mechanics*, vol. 24, no. 4, pp. 527–536, 2009.

[10] N. Alileche, V. Cozzani, G. Reniers, and L. Estel, "Thresholds for domino effects and safety distances in the process industry: A review of approaches and regulations," *Reliability Engineering and System Safety*, vol. 143, pp. 74–84, 2015.

[11] M. G. Zhang and J. C. Jiang, "An improved probit method for assessment of domino effect to chemical process equipment caused by overpressure," *Journal of Hazardous Materials*, vol. 158, no. 2-3, pp. 280–286, 2015.

[12] G. Atkinson, "Blast damage to storage tanks and steel clad buildings," *Process Safety and Environmental Protection*, vol. 89, no. 6, pp. 382–390, 2015.

[13] S. K. Clubley, "Long duration blast loading of cylindrical shell structures with variable fill level," *Thin-Walled Structures*, vol. 85, pp. 234–249, 2015.

[14] S. K. Clubley, "Non-linear long duration blast loading of cylindrical shell structures," *Engineering Structures*, vol. 59, pp. 113–126, 2015.

[15] V. Mittal, T. Chakraborty, and V. Matsagar, "Dynamic analysis of liquid storage tank under blast using coupled Euler-Lagrange formulation," *Thin-Walled Structures*, vol. 84, pp. 91–111, 2014.

[16] B. Y. Zhang, H. H. Li, and W. Wang, "Numerical study of dynamic response and failure analysis of spherical storage tanks under external blast loading," *Journal of Loss Prevention in the Process Industries*, vol. 34, pp. 209–217, 2015.

[17] A. Chen, L. A. Louca, and A. Y. Elghazouli, "Behaviour of cylindrical steel drums under blast loading conditions," *International Journal of Impact Engineering*, vol. 88, pp. 39–53, 2016.

[18] K. Hu and Y. Zhao, "Numerical simulation of internal gaseous explosion loading in large-scale cylindrical tanks with fixed roof," *Thin-Walled Structures*, vol. 105, pp. 16–28, 2016.

[19] D. Lv, W. Tan, L. Liu, G. Zhu, and L. Peng, "Research on maximum explosion overpressure in LNG storage tank areas,"

Journal of Loss Prevention in the Process Industries, vol. 49, pp. 162–170, 2017.

[20] J. Li, H. Hao, Y. Shi, Q. Fang, Z. Li, and L. Chen, "Experimental and computational fluid dynamics study of separation gap effect on gas explosion mitigation for methane storage tanks," *Journal of Loss Prevention in the Process Industries*, vol. 55, pp. 359–380, 2018.

[21] J. Li and H. Hao, "Far-field pressure prediction of a vented gas explosion from storage tanks by using new CFD simulation guidance," *Process Safety and Environmental Protection*, vol. 119, pp. 360–378, 2018.

[22] R. L. Zhang, J. J. Jia, H. F. Wang, and Y. H. Guan, "Shock response analysis of a large LNG storage tank under blast loads," *KSCE Journal of Civil Engineering*, vol. 22, no. 9, pp. 3419–3429, 2018.

[23] L. Jing, Z. H. Wang, and L. M. Zhao, "Dynamic response of cylindrical sandwich shells with metallic foam cores under blast loading-Numerical simulations," *Composite Structures*, vol. 99, pp. 213–223, 2013.

[24] LSTC, *LSDYNA Keyword User's Manual Version 971*, LSTC, Troy, MI, USA, 2007.

[25] S. Trélat, I. Sochet, B. Autrusson, K. Cheval, and O. Loiseau, "Impact of a shock wave on a structure on explosion at altitude," *Journal of Loss Prevention in the Process Industries*, vol. 20, pp. 509–516, 2007.

[26] S. Michelle, H. Fatt, and D. Sirivolu, "Blast response of double curvature, composite sandwich shallow shells," *Engineering Structures*, vol. 100, pp. 696–706, 2015.